



# Simulation of coupled transport of soil moisture and heat in a typical karst rocky desertification area, Yunnan Province, Southwest China

Xiaofeng Xiong<sup>1,2</sup> · Jianhong Li<sup>1</sup> · Tao Zhang<sup>1</sup> · Sainan Wang<sup>1</sup> · Weijie Huo<sup>1</sup>

Received: 7 May 2020 / Accepted: 9 September 2020 / Published online: 19 September 2020  
© Springer-Verlag GmbH Germany, part of Springer Nature 2020

## Abstract

Understanding the transport processes of soil moisture and heat is critical for vegetation restoration in karst rocky desertification areas where serious soil erosion and extensive exposure of carbonate rocks occur. Numerical simulation can provide an important approach to explore the transport processes of soil moisture and heat, but few studies employing this technique have been carried out in karst rocky desertification areas of southwest China. In this study, a model of coupled soil moisture and heat transport was established using HYDRUS-1D based on the high-resolution data of soil moisture, soil temperature, and meteorological parameters obtained throughout a year in a typical karst rocky desertification area in Yunnan province, southwest China. The modeling results reflect the rainfall-infiltration-evaporation processes in rocky desertification areas well. The frequently rainfall events in small intensity in the study site often induced great variations of soil moisture in the near-surface soil layer (< 1-cm depth). However, soil moisture in deep soil layer (> 10-cm depth) kept stable during light rainfall events, implying that the deep soil was only influenced by heavy rainfall events. The variations of soil temperature showed a high sinusoidal fitting trend. At the annual scale, variations of soil temperature were distinct apparent evident below the depth of 40 cm, but no evident daily variations were observed. The simulated fluxes of soil water showed that the vapor fluxes were lower than the liquid water fluxes by 3–6 orders of magnitude, suggesting the control of soil thermal gradients. Our results also indicate that the vapor flux has great significance for plant water utilization in the drought periods. The simulation errors are small for soil temperature but slightly more significant for the soil moisture in deep soil layer. This primary failure may result from the occurrence of preferential flows at the rock-soil interface, which needed to be further investigated in the future.

**Keywords** Karst rocky desertification area · In situ monitoring · Soil moisture · Soil temperature · Numerical simulation

## Introduction

Soil moisture and temperature coupling are an important subject in hydrology, agricultural science, and ecological research as they are critical factors affecting material and energy transport in a soil-plant-air system (SPAC) (Philip 1966; Hall and Kaufmann 1975; Federer 1979; Passioura 1982; Seneviratne

et al. 2010; Mahdavi et al. 2017). Areas with the occurrence of karst rocky desertification are characterized by soil discontinuity, high bedrock exposure rate, and serious soil erosion (Wang et al. 2004; Dai et al. 2017). Soil moisture and temperature are good indicators for soil degradation in the rocky desertification process and also are the limiting factors for agricultural development and ecological restoration. The slow formation of soil, shallow soil depths, and loose soil nature are the important reason for the low soil-loss tolerance and high soil erosion in the karst area (Jiang et al. 2014). Different from the soil and water loss in non-karst areas, which is mainly caused by slope loss, the process of soil and water loss in karst areas is very complicated. Sediment not only enters the flow system through surface runoff in the course of rainfall but also carries sediment into underground pipes and rivers through fall-water holes, shafts, and funnels (Bai et al. 2013; Jiang et al. 2014). So, water and energy transport along soil profiles are complicated in karst regions. Therefore, it is essential to

---

Responsible editor: Marcus Schulz

✉ Jianhong Li  
jianhongli1988@karst.ac.cn

<sup>1</sup> Key Laboratory of Karst Dynamics, MNR & Guangxi, Institute of Karst Geology, Chinese Academy of Geological Sciences, No. 50, Qixing Ave, Qixing District, Guilin 541004, China

<sup>2</sup> State Key Laboratory of Water Resources and Hydropower Engineering Science, Wuhan University, Wuhan 430072, China

conduct more investigations into soil moisture and temperature in rocky desertification areas (Chen et al. 2010). Previous studies have revealed that strong temporal and spatial variability of soil moisture and temperature often occurred in karst areas (Western and Blöschl 1999; Qiu et al. 2001; Western et al. 2004; Chen et al. 2010; Zhang et al. 2011; Vereecken et al. 2014; Yang et al. 2019) and there are preferential flows existing at rock-soil interface (Wilcox et al. 1988; Sohr et al. 2014; Zhao et al. 2018). However, researches on the processes and mechanism of soil water infiltration and energy transfers in the karst rock desertification area are still limited.

Commonly, in situ monitoring, physical modeling, and remote sensing are the primary techniques used to investigate soil moisture and temperature. The remote sensing has an advantage in obtaining data over a large area fast, but it just collects data of the surface moisture and temperature of the soil, limiting the vertical resolution of data (Kostov and Jackson 1993; Jackson et al. 1996; Zhang and Zhou 2016; Zhuo and Han 2016; Luo et al. 2019). However, the distribution of soil moisture and temperature along a soil profile is significant for microbial activity, ecological processes, and agricultural water supply (Dunn et al. 1985; Davidson et al. 1998; Zhang et al. 2009; Li et al. 2017; Smith et al. 2018). Traditionally, manual instruments were used to monitor the soil profile. Along with the time development, geophysical techniques such as ground-penetrating radar (GPR), electrical resistivity tomography (ERT), and wireless sensor network have been increasingly employed (Cardelloliver et al. 2005; Vereecken et al. 2014; Guo et al. 2015; Watlet et al. 2018). Guo et al. (2015) applied the time-lapse ground-penetrating radar to study the subsurface lateral preferential flow (LPF) and its dynamic characteristics. The long-term ERT monitoring of the water infiltration and recharge in the karst vadose zone was carried out by Watlet et al. (2018). The in situ method can accurately estimate soil moisture and temperature throughout the profile, but the monitoring data need to be combined with theoretical models for further analysis. There are numerous models for simulating water and heat transport in the vadose zone, such as the WAVE and CTSPAC models for agricultural engineering, the VS2D, SUTRA, and HYDRUS models for solving hydrological issues, the PORFLOW, FEMWATER, and 2DFATMIC models for environmental problems, and the TOPOG Dynamic and WAVES models for ecological problems (Jianfeng et al. 2005). Different models should be applied to a specified research field. The HYDRUS-1D is a finite element numerical simulation software package that can simulate soil water, heat, multiple solute transport, root water uptake, and CO<sub>2</sub> release process in variably saturated porous media (Simunek et al. 2005; Saito et al. 2006; Šimunek et al. 2016). Yet, it has been rarely used to simulate the coupled soil moisture and heat transport in the karst rocky desertification regions.

Yunnan province is one of the most vulnerable rocky desertification areas in southwest China, with the extent of rocky karst desertification about  $2.35 \times 10^4$  km<sup>2</sup>. Many projects on rocky desertification treatment, for example, the countermeasures used to prevent soil and water erosion, were carried out here (Li et al. 2016; Qiang et al. 2017). Therefore, understanding the transport processes of soil moisture and temperature is critical for ecological restoration in karst rocky desertification areas. In this study, a CR800 wireless weather station and soil moisture and temperature sensors have been installed along the soil profile in a typical karst rocky desertification area in Yunnan province. Based on the monitoring data, numerical simulation of coupled water and heat transport was performed using the HYDRUS-1D to estimate the water and heat flux in the soil profile. This study will contribute to a deep understanding of the ecological and hydrological process in the karst rocky desertification areas, and provide a guide for the rocky desertification treatment and ecological restoration.

## Materials and methods

### Study area

The Nandong Underground River System (NURS) is located in southeastern of Yunnan Province, China (Fig. 1a). The topography in the NURS area is mainly composed of a karst mountain and basin system, with the low karst basin surrounded by mountainous karst area (Fig. 1b). The altitude sharply decreases from the mountainous karst area (mean altitude of 2200 m a.s.l.) to the basin (mean altitude of 1250 m a.s.l.) within an east-west lateral distance of about 2 km (Li et al. 2020). This area is mainly underlain by rocks of the Triassic Gejiu formation (T2g), which consists of thick limestone and dolomite units. Carbonate rocks cover about 950 km<sup>2</sup>, or 58.7% of the total area, and limestone and dolomite each comprise approximately 50% of the carbonate rocks (Jiang 2011). There are some karst springs or underground river on the margin of the basin. The mountainous karst area with altitude of about 2200 m (Fig. 1b) is an ancient planation surface with wide outcrops of middle Triassic carbonate rock (Gejiu formation). There are five land use types in the NURS: forested land, grassland, cultivated land, water bodies, and construction land (towns and other urbanized areas). In 2010, the percentages of land use for each type were 50% cultivated land, 13.4% forested land, 30.43% grassland, 2.45% construction land, and 2.62% water bodies (Li et al. 2020). Sinkholes are ubiquitous and located in the bottom of the depressions in the mountainous karst area, approximately 30 sinkholes per square kilometer. In the mountainous karst area, soil erosion and water leakage are serious ecological environment issues, resulting in severe karst rocky desertification and water shortage.

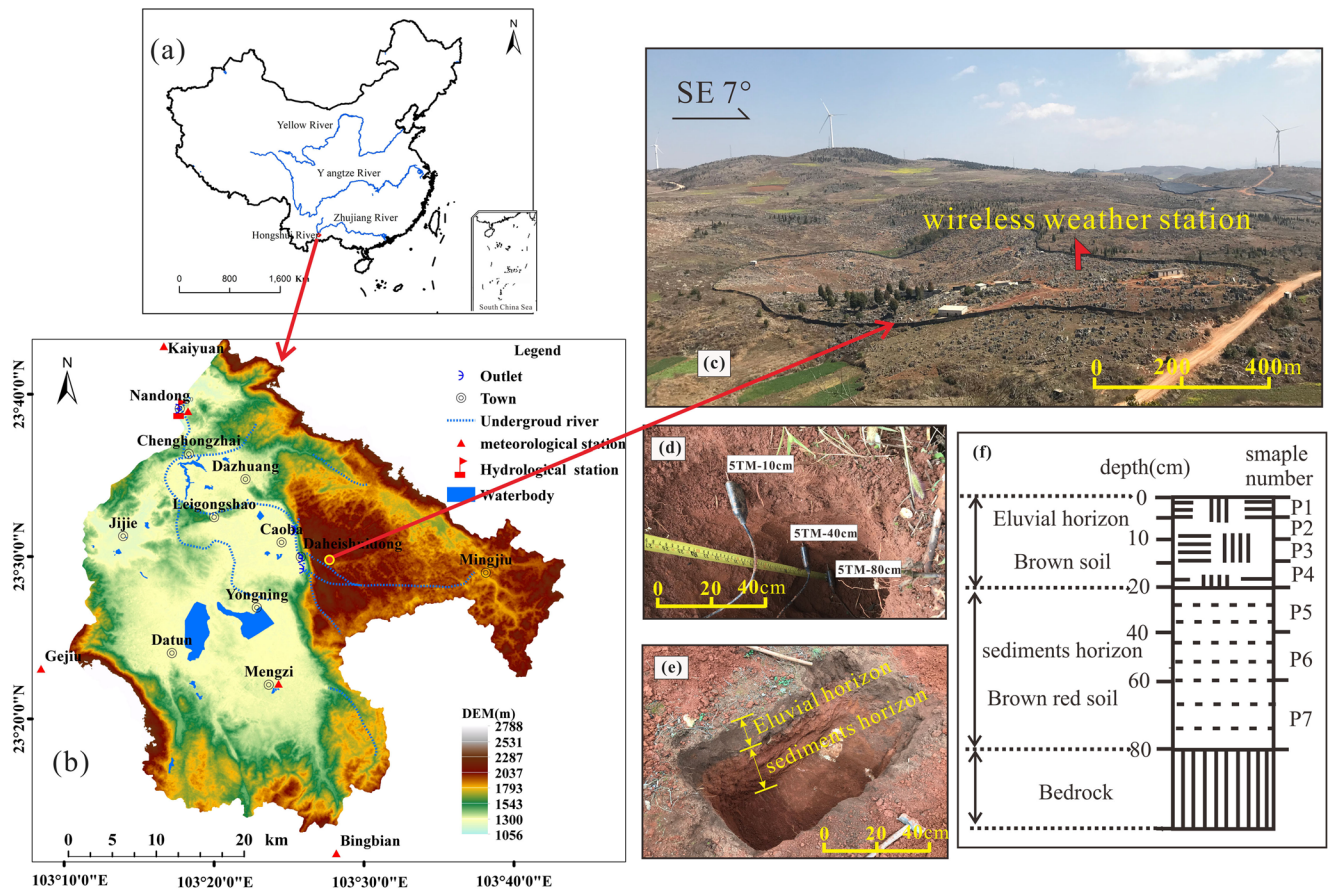


**Fig. 1** a Location of the study area, b DEM image of the Nandong Underground River Basin, c bird view of the study site, d monitoring sensors embedded along the soil profile, and e, f soil profile depictions

This region has a subtropical monsoon climate with obvious dry and wet seasons. The average annual rainfall is 831 mm and the mean air temperature is 19.5 °C, and most rainfall occurs during July–October (Jiang 2011). Under the influence of graben basin topography, the vertical variation of meteorological parameters in NURS is obvious. Annual rainfall is the highest on the mountainous karst area (1027.4 mm), followed by the basin (662.6 mm), and the lowest on the transitional hillslope (574.4 mm). The topographic relief makes the annual variation coefficient of rainfall in the basin reached 152.36%, which is much larger than the hillside (113.81%) and the mountain (99.36%), and amplifies the change of “dry and wet” in the vertical direction. In addition, in mountainous areas of karst graben basins, light rainfall event with short occurrence takes a big proportion in annual precipitation (Li et al. 2019). The aridity index shows that the basin is the highest (1.74), the transitional hillslope is the second (1.70), and the mountain area is the lowest (0.88) (Wang et al. 2019).

For understanding the variations of soil moisture and temperature, this study established an *in situ* monitoring station in the mountainous karst area, which is located in an apple orchard near Xibeile village (103° 27' 14.19", 23° 26' 57.22";

Fig. 1c). The exposure rate of carbonate rock in this apple orchard reaches up to 45–65%.

### Filed monitoring

The CR800 wireless weather station (Campbell Company, USA) was installed in the study site. The 5TM soil moisture and temperature sensor (Decagon Company) were connected to the data collector in the weather station. According to the actual soil structure in the site, we installed the sensors at the depth of 10 cm, 40 cm, and 80 cm (Fig. 1d). Precipitation, atmospheric pressure, atmospheric vapor pressure, air temperature, air humidity, solar radiation, wind speed, wind direction, soil water content, and soil temperature were automatically logged by the weather station at a time interval of 30 min. Because it is possible that the natural structure of soil has been disturbed when embedding the sensors, we only use the data collected after 2 months when the sensors were installed. A 365-day time series data from 01/01/2017 to 31/12/2017 were processed in this study. In order to analyze the data conveniently, this study used the daily cumulative values of precipitation and solar radiation. The other meteorological

**Table 1** Physical properties of soil samples

Sample number	Silt (%; 2–50 μm) Mean	Clay (%; < 2 μm) Mean	Sand (%; 50–2000 μm) Mean	ρ (g cm <sup>-3</sup> ) Mean	θ (cm <sup>3</sup> cm <sup>-3</sup> ) Mean
P1	48.4	39.2	12.4	1.15	30.8
P2	46.9	36.3	16.8	1.20	34.5
P3	50.5	39.1	10.4	1.00	26.3
P4	56.6	25.6	17.8	1.35	40.6
P5	54.7	28.6	16.7	1.32	30.8
P6	46.5	42.8	10.7	1.35	22.6
P7	42.7	42.4	14.9	1.32	20.4

data, such as air temperature and air humidity, were processed using average daily value.

Well-preserved soil profiles with grass cover are sampled near the weather station on August 20, 2017 (Fig. 1c). The soil profile stratification is obvious (Fig. 1e). The upper layer (0–20 cm) is an eluvial horizon with higher organic matter content and loose soil texture. In the eluvial horizon (0–20 cm), a composite sample was taken for every 5 cm (Fig. 1f, P1 0–5 cm, P2 5–10 cm, P3 10–15 cm, P4 15–20 cm). The lower layer (20–80 cm) is a sediment horizon with stronger viscosity. In the sediment horizon (20–80 cm), a composite sample was taken for every 20 cm (Fig. 1f, P5 20–40 cm, P6 40–60 cm, P7 60–80 cm). The physical properties of these soil samples, such as the composition of grain size (silt, clay, and sand), bulk density (ρ), and natural moisture (θ, soil moisture is expressed by soil volumetric water content in this study), were tested at the Environmental and Geochemical Analysis Laboratory of the Institute of Karst Geology, Chinese Academy of Geological Sciences. The basic physical properties of soil samples are listed in Table 1. According to the UNSODA database chart (Nemes et al. 2001), the soil textures are plotted in Fig. 2, which shows that the soil textures of the samples are mainly silty clay loam and silty clay.

**Filed data analyses**

**Evapotranspiration calculation**

There are numerous methods to calculate potential evapotranspiration ( $ET_p$ ) (Xu and Singh 2001). This study chooses the Penman-Monteith equation which is recommended by the Food and Agriculture Organization of the United Nations (FAO). The Penman-Monteith equation is often adopted when dealing with long-term monitoring and meteorological data based on the energy balance and water vapor diffusion theory (Monteith 1981; Valipour et al. 2017). The equation uses assumed plant type and geographical coordinates of the monitoring site, combined

with radiation and aerodynamic conditions, to deduce high accuracy results. It is expressed as

$$ET_p = \frac{0.408\Delta(R_n - G) + \beta \frac{900}{T + 273} u_2 (e_s - e_a)}{\Delta + \beta(1 + 0.34u_2)} \quad (1)$$

where  $ET_p$  is the reference evapotranspiration (mm day<sup>-1</sup>),  $\Delta$  is the slope vapor pressure curve (kPa °C<sup>-1</sup>),  $R_n$  is the net radiation at the crop surface (MJ m<sup>-2</sup> day<sup>-1</sup>),  $G$  is the soil heat flux density (MJ m<sup>-2</sup> day<sup>-1</sup>),  $T$  is the mean daily air temperature at 2-m height (°C),  $u_2$  is the wind speed at 2-m height (m s<sup>-1</sup>),  $e_s$  is the saturation vapor pressure (kPa),  $e_a$  is the actual vapor pressure (kPa),  $\beta$  is the psychrometric constant (kPa °C<sup>-1</sup>). In most cases, the estimation of  $G$  is minimal compared to  $R_n$  and thus can be ignored. We used the  $ET_O$  software (Raes and Munoz 2009) to calculate  $ET_p$ . The input parameters of  $ET_O$  are meteorological data which can be directly obtained from the weather station.

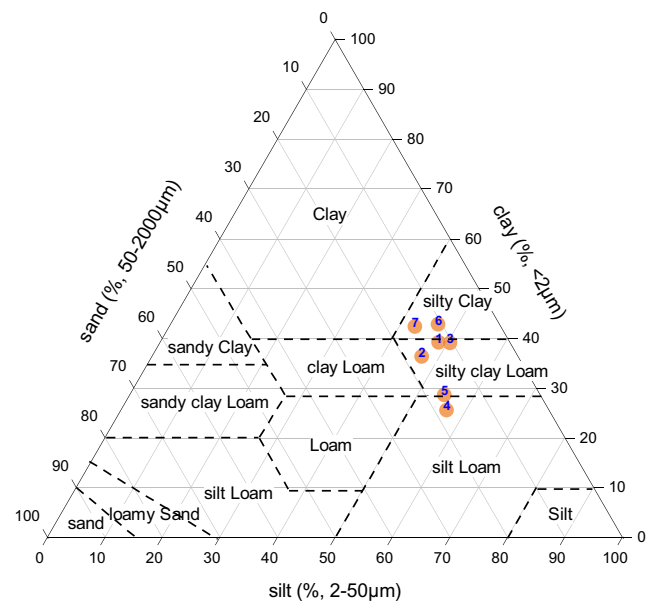


**Fig. 2** Soil textures of samples in the UNSODA database triangular chart (Nemes et al. 2001)



## Soil temperature fitting

Commonly, shallow soil heat is derived from solar radiation. Autobiography and revolution of the Earth cause changes in solar radiation intensity at diurnal to annual time scales, thereby inducing the sinusoidal cycle for soil temperature and air temperature in the time series (Parton and Logan 1981; Kang et al. 2000). Bhumralkar (1975) assumed that air temperature and surface soil temperature obey sinusoidal periodic distribution. The formula can be expressed as

$$T_s(t) = \bar{T} + \Delta T_0 \sin(\omega t + \varphi) \quad (2)$$

where  $\bar{T}$  is the average temperature (°C),  $\Delta T_0$  is the temperature amplitude (°C),  $\omega$  is the frequency of oscillation expressed as  $\omega = 2\pi/p$ , and  $p$  represents the period of the wave.  $\varphi$  is the phase of the wave. Assuming that the soil is homogeneous and heat flow is only in the vertical direction, the heat conduction equation can be solved with method of separation of variables. The soil temperature along the profile can be expressed with an analytical formula:

$$T_s(z, t) = \bar{T} + \Delta T_0 e^{-z/d} [\sin(\omega t - z/d)] \quad (3)$$

where  $d = (2\lambda/c\omega)^{1/2}$  is the depth where the soil temperature amplitude is closed to zero. The value of  $d$  in the mid-latitude area often exceeds 15 m. In this study, the temperature was measured within 1 m in the filed site; this depth of the soil can also be regarded as surface soil of the ground. The term  $e^{-z/d} \approx 1$ . Therefore, it is better to fit the soil temperature using Eq. [2]

## Soil water and heat transport simulation model

### Governing equations

Water and heat transport in soil is a quite complex process, and in most cases, they are coupled with vapor flow and thermal effects. In the arid and semiarid regions, the thermal vapor flux may dominate in the total water flux (Scanlon et al. 2003; Šimůnek et al. 2012). Thus, the water movement in the soil should involve the isothermal liquid flow, isothermal vapor flow, gravitational liquid flow, thermal liquid flow, and thermal vapor flow. This study neglects the water uptake by roots due to the low vegetation coverage around the monitoring site. The modified mass balance Richards equation for a vertical profile can be expressed as

$$\frac{\partial \theta_T(h)}{\partial t} = \frac{\partial}{\partial z} \left[ (K_{Lh} + K_{vh}) \frac{\partial h}{\partial z} + (K_{LT} + K_{vT}) \frac{\partial T}{\partial z} \right] \quad (4)$$

where  $\theta_T$  is the total volumetric water content ( $\text{m}^3 \text{m}^{-3}$ ),  $h$  is the water pressure head in the vadose zone (m),  $T$  is the soil temperature (°C),  $K_{Lh}$  ( $\text{m s}^{-1}$ ), and  $K_{vh}$  ( $\text{m s}^{-1}$ ) are isothermal hydraulic conductivities for liquid and vapor respectively,  $K_{LT}$

( $\text{m}^2 \text{K}^{-1} \text{s}^{-1}$ ) and  $K_{vT}$  ( $\text{m}^2 \text{K}^{-1} \text{s}^{-1}$ ) are thermal conductivities for liquid and vapor under thermal gradients. The variables of  $K_{LT}$ ,  $K_{vh}$ , and  $K_{vT}$  can be defined as

$$\begin{aligned} K_{LT}(T) &= K_{Lh}(h) \left( h G_{wT} \frac{1}{\gamma_0} \frac{d\gamma}{dT} \right); K_{vh} \\ &= \frac{D_v}{\rho_w} \rho_{vs} \frac{Mg}{R_u T} H_r; K_{vT} = \frac{D_v}{\rho_w} \eta_e H_r \frac{d\rho_{vs}}{dT} \end{aligned} \quad (5)$$

where  $G_{wT}$  is the grain factor (unitless),  $\gamma$  is the surface tension of soil water ( $\text{J m}^{-2}$ ),  $\gamma_0$  is the surface tension at 25 °C ( $= 71.89 \text{ g s}^{-2}$ ),  $\gamma$  can be expressed as  $\gamma = 75.6 - 0.1425 T - 2.38T^2/10^4$  ( $\gamma$  is in  $\text{g s}^{-2}$ , and  $T$  is in °C).  $D_v$  is the vapor diffusivity in soil ( $\text{m}^2 \text{s}^{-1}$ ),  $\rho_{vs}$  is the saturated vapor density ( $\text{kg m}^{-3}$ ),  $M$  is the molecular weight of water ( $M = 0.018015 \text{ kg mol}^{-1}$ ),  $g$  is the gravitational acceleration ( $= 9.81 \text{ m}^2 \text{s}^{-1}$ ),  $R_u$  is the universal gas constant ( $R_u = 8.314 \text{ J mol}^{-1} \text{K}^{-1}$ ),  $\eta_e$  is the enhancement factor (unitless), and  $H_r$  is the relative humidity (unitless). Some details about variables' definition can be found in the previous studies (Cass et al. 1984; Nimmo and Miller 1986).

Soil heat convection-dispersion equation in the vertical profile was described in Nassar and Horton (1992) and Saito (2006):

$$\begin{aligned} C_p(\theta) \frac{\partial T}{\partial t} + L_0 \frac{\partial \theta_v}{\partial t} \\ = \frac{\partial}{\partial z} \left( \lambda(\theta) \frac{\partial T}{\partial z} \right) - C_w q \frac{\partial T}{\partial z} - C_v \frac{\partial q_v T}{\partial z} - L_0 \frac{\partial q_v}{\partial z} \end{aligned} \quad (6)$$

In the equation, the first term on the right side is defined as the conduction of sensible heat by Fourier's law, and the second term is the convection of sensible heat by liquid flow, the third term is the convection of water vapor, and the fourth term is the convection of latent heat by vapor flow. In terms of variables,  $C_p(\theta)$ ,  $C_w$ , and  $C_v$  are volumetric heat capacities of the porous media, liquid phase, and vapor phase ( $\text{J m}^{-3} \text{°C}^{-1}$ ), respectively.  $T$  is the soil temperature (°C),  $L_0$  is the volumetric latent heat of vaporization of liquid phase ( $\text{J m}^{-3}$ ), and  $\theta_v$  is the volumetric vapor content ( $\text{m}^3 \text{m}^{-3}$ ),  $\lambda(\theta)$  is the apparent thermal conductivity of soil ( $\text{J m}^{-1} \text{s}^{-1} \text{°C}^{-1}$ ),  $q$  and  $q_v$  are flux density of liquid water and water vapor ( $\text{m s}^{-1}$ ), respectively. The  $q_v$  can be expressed as

$$q_v = -K_{vh} \left( \frac{\partial h}{\partial z} + 1 \right) - K_{vT} \frac{\partial T}{\partial z} \quad (7)$$

The variables in this equation are the same as Eq. [4].

### Initial and boundary conditions

After the establishment of soil water and heat transport model based on filed conditions along the vertical profile, the

HYDRUS-1D package software was used to solve the governing equations in finite element method for spatial discretization and finite difference for temporal discretization (Simunek et al. 2005; Saito et al. 2006). The total length of the profile is 100 cm, and at the surface  $z = 0$  m and  $z = 100$  cm at the bottom. The profile was discrete into 100 grids with a constant nodal space of 1 cm. The soil textures at the depth of 0–15 cm are silty loam, and 15–100 cm are silty clay. The initial conditions in the model mainly include soil water content and soil temperature, and they can be given as

$$\theta(z, t) = \theta_0(z), \quad t = 0, z = z_i \tag{8}$$

$$T(z, t) = T_0(z), \quad t = 0, z = z_i \tag{9}$$

where  $\theta_0$  is the initial soil volumetric water content ( $\text{m}^3 \text{m}^{-3}$ ) and  $T_0$  is the initial soil temperature ( $^\circ\text{C}$ ). The  $z_i$  is the depth of the observation point ( $z_1=10$  cm,  $z_2=40$  cm,  $z_3=80$  cm). Because the initial conditions of soil moisture and temperature have some impacts on soil water movement, the measured data on the first day was used and interpolated linearly into the soil profile. The initial soil moisture and temperature are shown in Fig. 3.

The terms of sources and sinks in the model are precipitation, potential evapotranspiration, and deep drainage. The potential evapotranspiration was calculated by the Penman-Monteith formula. We neglected the root water uptake, because there are weeds around the monitoring site, and the weed roots are shallow in the soil. The soil-air interface was considered as an atmospheric boundary with surface runoff.

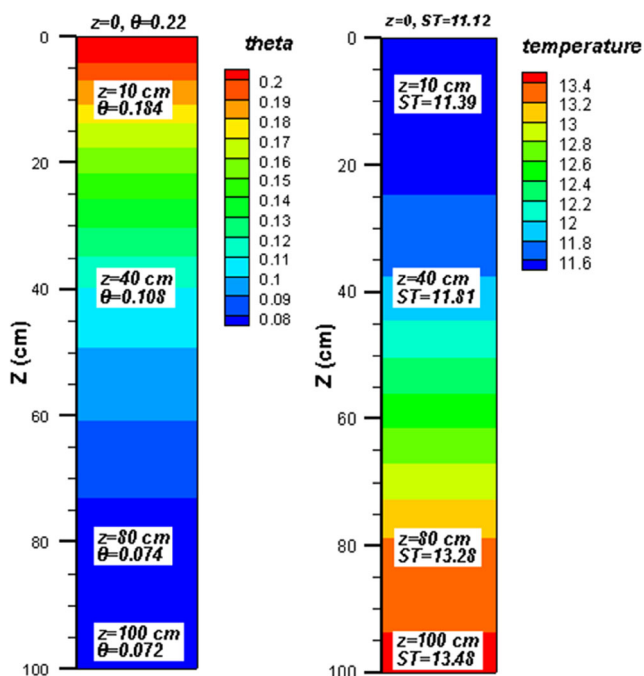


Fig. 3 Initial conditions of soil water content and soil temperature on the profile

The bottom of the profile was considered as a free drainage boundary. The surface boundary can be given as

$$-K \frac{\partial h}{\partial z} = q_0(t), \quad t \geq 0, z = 0 \tag{10}$$

where  $q_0$  is the soil surface flux including infiltration and evapotranspiration. Assuming that the free drainage boundary at the bottom has a zero gradient of water head pressure, then it can be given as

$$\frac{\partial h(z, t)}{\partial z} = 0, \quad t \geq 0, z = L \tag{11}$$

In terms of temperature boundary, the heat flux boundary can be applied to the surface, but it is too complex and needs many parameters, so we take the measured soil temperature at  $z = 10$  cm (Dirichlet type) as the surface boundary. The bottom was considered as a thermal zero gradient (Neuman type) boundary which can be expressed as

$$\frac{\partial T(z, t)}{\partial z} = 0, \quad t \geq 0, z = L \tag{12}$$

### Model parameterization

The model parameters mainly include soil hydraulic, heat conductive properties, and numerical solution parameters. The soil water retention curve (WRC) plays a critical crucial role in soil water and solution transport. The most widely used empirical models for describing WRC are Gardner, Brooks-Corey (BC), and van Genuchten (VG) model. The VG model belongs to the pedotransfer function method, based on semi-empirical theory, and has been applied to a wide range of soil textures (Mualem 1976; Van Genuchten 1980). This study uses the van Genuchten-Malem (VGM) model to predict the hydraulic parameters. The input data for the VGM model are soil particle grading and soil density. This study selected the RETC code as an efficient tool. The equation of the VGM model can be expressed as

$$\theta(h) = \begin{cases} \theta_r + \frac{\theta_s - \theta_r}{[1 + |\alpha h|^n]^m} & h < 0 \\ \theta_s & h \geq 0 \end{cases} \tag{13}$$

$$K(h) = K_s S_e^l \left[ 1 - \left( 1 - S_e^{1/m} \right)^m \right]^2 \tag{14}$$

where  $\theta(h)$  is the volumetric water content ( $\text{m}^3 \text{m}^{-3}$ ) and  $h$  is the water pressure head (m).  $\theta_s$  and  $\theta_r$  are saturated and residual water content ( $\text{m}^3 \text{m}^{-3}$ ), respectively.  $\alpha$  ( $\text{m}^{-1}$ ),  $n$  (unitless), and  $m$  ( $m = 1 - 1/n$ ) are empirical parameters.  $K(h)$  and  $K_s$  are unsaturated and saturated hydraulic conductivity ( $\text{m s}^{-1}$ ) respectively,  $S_e^l$  is the adequate saturation (unitless), and  $l$  is the pore-connectivity parameter given a value of 0.5

usually. Previous studies have shown that the  $n$  and  $\alpha$  are the most sensitive parameters in the VG model while  $\theta_r$  is insensitive to the WRC (Younes et al. 2013).

The soil heat capacity and thermal conductivity are key parameters in the heat transport equation. The soil heat capacity  $C(\theta)$  can be expressed as

$$C(\theta) = C_n\theta_n + C_o\theta_o + C_w\theta_w + C_g\theta_g \quad (15)$$

$$\approx (1.92\theta_n + 2.51\theta_o + 4.18\theta) \times 10^6$$

where  $\theta$  is volumetric friction ( $\text{m}^3 \text{m}^{-3}$ ),  $C$  is the volumetric heat capacity ( $\text{J m}^{-3} \text{ }^\circ\text{C}^{-1}$ ), the subscripts  $n$ ,  $o$ ,  $w$ , and  $g$  represent solid phase, organic matter, gas phase, and liquid phase respectively. The apparent thermal conductivity  $\lambda(\theta)$  combines the thermal conductivity  $\lambda_0(\theta)$  of the porous media in the absence of flow and the macro-dispersivity (Saito et al. 2006; Šimůnek et al. 2012).  $\lambda(\theta)$  can be expressed as

$$\lambda(\theta) = \lambda_0(\theta) + \beta_T C_w |q_L| \quad (16)$$

where  $\beta_T$  is the thermal dispersivity (m),  $C_w$  is the volumetric heat capacity for the liquid phase ( $\text{J m}^{-3} \text{ }^\circ\text{C}^{-1}$ ), and  $q_L$  is the flux density of liquid water ( $\text{m s}^{-1}$ ). In this study, the Chung and Horton (1987) equation was used to describe the thermal dispersivity (Chung and Horton 1987):

$$\lambda_0(\theta) = b_1 + b_2\theta + b_3\theta^{0.5} \quad (17)$$

where  $b_1$ ,  $b_2$ , and  $b_3$  are empirical parameters ( $\text{W m}^{-1} \text{ }^\circ\text{C}^{-1}$ ). In most cases, the thermal dispersion effect can be neglected for little liquid water flux, and only  $\lambda_0(\theta)$  will be considered. So the key parameters in the heat transport process are  $b_1$ ,  $b_2$ , and  $b_3$ , and they have been given by Chung and Horton (1987) for three texture soils (i.e., clay, loam, and sand) (Chung and Horton 1987). Other parameters like  $C_n$ ,  $C_o$ ,  $C_w$ ,  $\theta_n$ ,  $\theta_o$ , and  $\beta_T$ , we can use literature values from previous studies (Chung and Horton 1987; Saito et al. 2006; Wang et al. 2013). In this study, the centimeter (cm) for length and day for time unit was used in HYDRU-1D, so other parameters should keep consistent. The parameters for the water and heat transport model are summarized in Table 2.

## Results and discussion

### Precipitation and evapotranspiration

MATLAB was used to process the recorded precipitation data to obtain the distribution of rainfall time interval, rainfall duration, rainfall amount, and rainfall density. The rainfall after 2 h without the recording of data would be judged as a new rainfall event. The 1-year precipitation data were analyzed with the statistical approach. The statistical data for rainfall attributes are shown in Fig. 4 and Table 3. The annual cumulative precipitation is 1027.2 mm, and precipitation concentrates on a period from June to August when the total precipitation is 624.0 mm (60.7% of 1 year). Total 381 rainfall events, with the highest single rainfall event of 45.4 mm and the highest rainfall intensity of 9.52 mm/h, were recognized. The biggest time-interval between two different rainfall events is 289.5 h. The frequency of rainfall duration showed that duration of 0.5–1.5 h accounted for 64.6% with 246 times. The frequency of 0.2–2.2 mm rainfall amount and 0.2–0.6 mm/h rainfall intensity is 289 times and 255 times, which accounted for 75.9% and 66.9%, respectively. These rainfalls are frequent, short, and have low intensity in the mountainous karst area. This is one of the reasons why the surface soil moisture fluctuates rapidly but the deep soil can hardly get water recharged from the rains.

Although the precipitation has an intense temporal variability, the potential evapotranspiration has a fairly uniform distribution throughout the whole year (Fig. 5). The annual cumulative potential evapotranspiration is 901.4 mm and has little difference in all seasons (Fig. 6). In general, the characteristics of precipitation and evapotranspiration in the mountainous karst area determine the soil moisture variability combined with soil texture classes. Due to the impacts of small rainfall events, most of the precipitation reaches the surface soil layer and increases the surface soil moisture. Thus, the rainwater infiltration depth is limited. The deeper soil can only get rainwater supply in the concentrated rainfall period (July–August).

**Table 2** Main parameters for the numerical simulation model

VGM parameters	Value (silty loam)	Value (silty clay)	Chuang-Horton parameters	Value (silty loam)	Value (silty clay)	Additional parameters	Value
$\theta_s$ ( $\text{cm}^3 \text{cm}^{-3}$ )	0.51	0.44	$\theta_n$ ( $\text{cm}^3 \text{cm}^{-3}$ )	0.57	0.62	$C_n$ ( $\text{J m}^{-3} \text{ }^\circ\text{C}^{-1}$ )	1.4
$\theta_r$ ( $\text{cm}^3 \text{cm}^{-3}$ )	0.09	0.078	$\theta_o$ ( $\text{cm}^3 \text{cm}^{-3}$ )	0.01	0	$C_o$ ( $\text{J m}^{-3} \text{ }^\circ\text{C}^{-1}$ )	1.9
$\alpha$ ( $\text{cm}^{-1}$ )	0.0105	0.0063	$\beta_T$ (cm)	5	7	$C_w$ ( $\text{J m}^{-3} \text{ }^\circ\text{C}^{-1}$ )	3.1
$n$	1.46	1.56	$b_1$ ( $\text{kg cm day}^{-3} \text{ }^\circ\text{C}^{-1}$ )	$1.6 \times 10^{16}$	$-1.3 \times 10^{16}$	$t_{\text{step}_{\text{max}}}$ (days)	1
$l$	0.5	0.5	$b_2$ ( $\text{kg cm day}^{-3} \text{ }^\circ\text{C}^{-1}$ )	$2.5 \times 10^{16}$	$-6.2 \times 10^{16}$	$t_{\text{step}_{\text{min}}}$ (days)	$1\text{E}-5$
$K_s$ (cm/day)	39.5	14.6	$b_3$ ( $\text{kg cm day}^{-3} \text{ }^\circ\text{C}^{-1}$ )	$9.9 \times 10^{16}$	$1.6 \times 10^{17}$	$T_{\text{max}}$ (days)	365

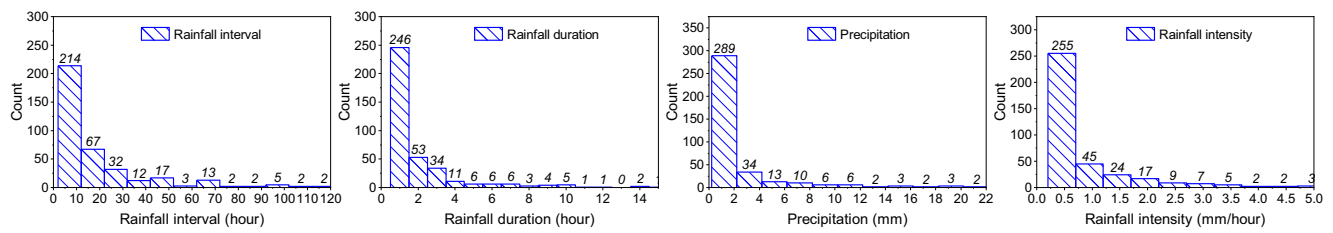


Fig. 4 Statistical histogram of rainfall interval, rainfall duration, rainfall amount, and rainfall intensity

Table 3 Distribution statistics for rainfall attribute

Variables	Min	Max	Main range	Frequency within the main range	Percentage
Rainfall interval (h)	2	289.5	2–12	214	56.2
Rainfall duration (h)	0.5	24.0	0.5–1.5	246	64.6
Precipitation (mm)	0.2	45.4	0.2–2.2	289	75.9
Rainfall density (mm/h)	0.4	9.52	0.4–0.6	255	66.9

### Soil temperature fitting results

The soil temperatures at different depths were fitted by sinusoidal curves (Fig. 7). From the fitting results, we found that (1) temperature and soil temperature at a depth of 10 cm showed the same trend but slightly lagged (Fig. 7a). This trend implies that the surface soil temperature was mainly affected by the air temperature. But the soil temperature at depth of 40 cm and 80 cm almost shows no fluctuation and present nearly a straight line, which indicates that they are hardly affected by the temperature difference between day and night. The dynamic regulation of soil temperature at different depths are in accord with previous studies which were revealed that the soil temperature would present an exponential decay along the profile, and the amplitude of the variation of soil temperature in a day is inconspicuous when the depth exceeds 30–60 cm and thus only clear annual amplitude of variation can be observed (Carson 1963; Jaynes 1990; Shao et al. 1998); (2) at the aspect of annual variation, soil temperature increases with depth in both 0–39 days and 253–365 days, while in other periods, it decreases with depth (Fig. 7b).

The fitting parameters are listed in Table 4. The determination coefficient ( $R^2$ ) reflects the accuracy of curve fitting. The  $R^2$  has a low value of 0.34 for soil temperature at 80 cm,

which implies that the deeper soil has experienced subtle influence from the air temperature and weak sinusoidal trend. For daily average soil temperature throughout the year, the  $R^2$  increase with depth, which can also indicate the deep soil temperature is relatively stable and has subtly influenced by the variable air temperature but may be influenced by climate change throughout the year. All soil temperature dynamic regulations are related to the Earth’s rotation and revolution.

### Numerical simulation results and model evaluation

The comparison of simulated and measured soil water content is shown in Figs. 8 and 9. The soil moisture simulation results match the measured values greatly at the depth of 10 cm, while the difference is larger at 40 cm and 80 cm. Soil temperature shows highly consistent at all three depths of 10 cm, 40 cm, and 80 cm. The soil moisture simulation accuracy cannot be improved effectively in this study, as the soil moisture has many influencing factors, such as precipitation, evapotranspiration, soil textures, and the dominant channel for infiltration between soil and rock. In the karst desertification areas, the preferential flow at the interface between soil and rock may contribute a lot to the deeper soil moisture (Li et al. 2014; Sohrt et al. 2014; Jarvis et al. 2016; Zhao et al. 2018). We still need more evidence to verify this conclusion.

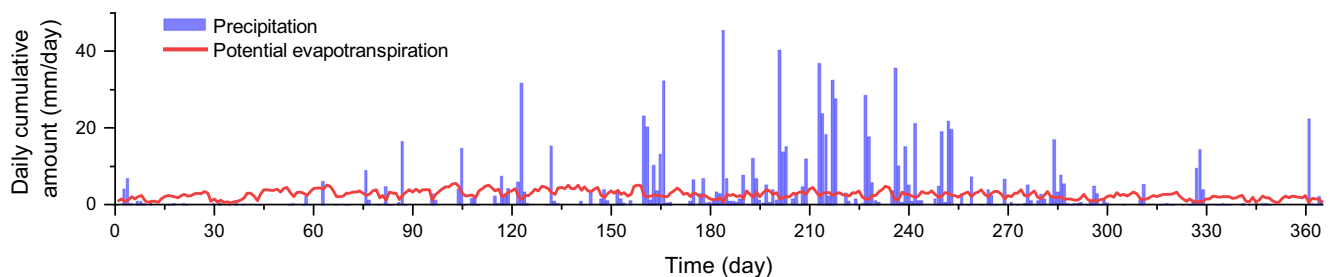
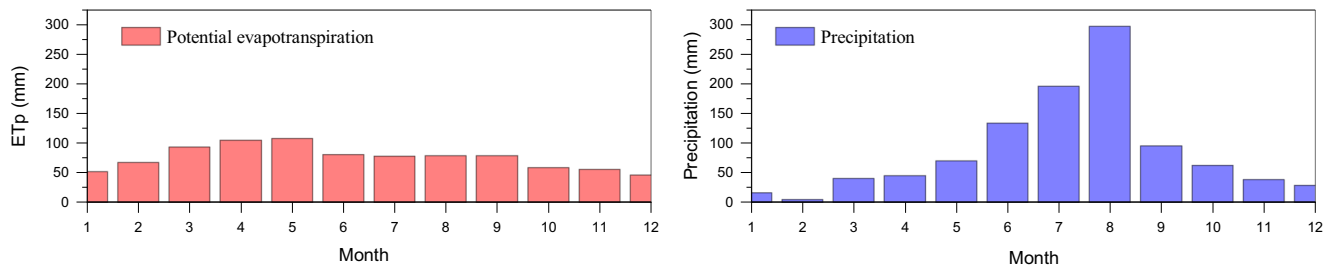


Fig. 5 Variations of precipitation and potential evapotranspiration within 1 year





**Fig. 6** Cumulative monthly rainfall and evapotranspiration histogram

Automatic steps were adopted in the model, and the print-out times were set to 1 day in order to compare with the measured data. Here, we use the Nash-Sutcliffe efficiency (*NSE*) coefficient, root-mean-square error (*RMSE*), and relative root mean square error (*RRMSE*) to evaluate the model and simulation error. They can be expressed as

$$NSE = 1 - \frac{\sum_{i=1}^N (M_i - C_i)^2}{\sum_{i=1}^N (C_i - \bar{C})^2}, \quad RMSE = \sqrt{\frac{\sum_{i=1}^N (M_i - C_i)^2}{N}}$$

$$RRMSE = \frac{RMSE}{C_{\max} - C_{\min}}$$

where  $N$  is the number of measured data,  $M_i$  is the simulated value,  $C_i$  is the measured average daily value.  $C_{\max}$  and  $C_{\min}$  are the maximum and minimum of  $C_i$  respectively. The value of *NSE* varies from  $-\infty$  to 1, and indicates that the model is highly accurate when the *NSE* is between 0 and 1. The model will be unreliable if *NSE* is much less than 0. *NSE* is not suitable for judging the quality of the model alone (Willmott 1981, 1982), so *RMSE* and *RRMSE* were used as a reference. The model is reliable when *RMSE* and *RRMSE* are closed to zero. when  $RRMSE < 10\%$  the model performance can be evaluated as “excellent,”  $10\% < RRMSE < 20\%$  as “good,”  $20\% < RRMSE < 30\%$  as “acceptable,” and  $30\% < RRMSE$  will be evaluated as “poor.”

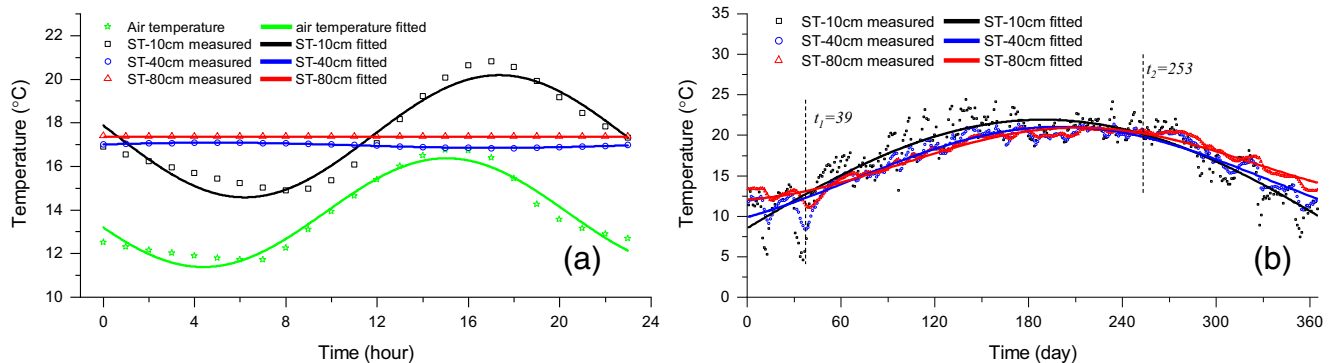


**Fig. 7** Empirical formula fitting of air temperature and soil temperature at different depths. **a** Daily fitting with average hourly data, **b** annually fitting with average daily data

The value of *NSE*, *RMSE*, and *RRMSE* are listed in Table 5. In the table, the value of *NSE* for *SWC* are 0.73 and  $-0.04$  at the depth of 10 cm and 80 cm respectively, which implies the reliable simulation results, but the *NSE* value is  $-1.78$  at 40 cm, which means a slightly big error for simulation results. All *NSE* values for *ST* are close to 1, which means high precision for *ST* simulation results. We can conclude from the *RMSE* and *RRMSE* that the model performance can be accepted within the normal error tolerance because the value of *RRMSE* is within 20% for all depth of *SWC* and *ST*. After all, the *HYDRUS-1D* model established in this study can be used to understand the process of soil water and heat transport on the soil profile.

### Water flux and vapor transport on the soil profile

An important function of the model is to provide flux and velocities at some observation points. The daily average fluxes of liquid water at different depths in the whole year are shown in Fig. 10, as well as the volume of water storage in the model. The actual surface flux seems the same as the flux at  $z = 10$  cm, and the flux decreases intensely with depth. We can deduct from the curves that the deeper soil can only get water recharged when the rains are heavy and concentrate in a short period (from June to August). The fluxes at the observation points are the combined results of model input (rainfall) and output (surface evapotranspiration, bottom leakage) (Sala et al. 1992). The summation of the volume of water

**Table 4** Air temperature and soil temperature fitting parameter and determination coefficients

	$\bar{T}$	$\Delta T_0$	$\omega$	$\varphi$	$R^2$
Average hourly temperature in a day					
Air temperature	13.73	2.480	0.2918	- 2.83	0.95
$T_{10\text{cm}}$	17.39	2.807	0.2815	- 3.31	0.93
$T_{40\text{cm}}$	16.96	0.120	0.2578	0.31	0.99
$T_{80\text{cm}}$	17.37	0.002	0.2513	1.83	0.34
Average daily temperature in a year					
$T_{10\text{cm}}$	17.39	5.52	0.0162	- 1.51	0.76
$T_{40\text{cm}}$	16.96	4.74	0.0162	- 1.70	0.88
$T_{80\text{cm}}$	17.37	4.01	0.0162	- 1.87	0.93

storage in the model varied with time and reached the summit point during periods of concentrated rainfall.

The cumulative water flux was calculated with temporal water flux (Fig. 11). The precipitation and infiltration are assumed to be the positive scalar, and other variables are vector (positive when migrating upwards such as the actual evaporation and negative when migrate downwards such as flux). The surface runoff of the model turns out to be zero for the small rains; therefore, the cumulative precipitation equals to the cumulative infiltration throughout the whole year, which implies that all precipitation has infiltrated into the soil. This phenomenon may result from two reasons: (1) The HYDRUS numerical simulation has certain errors. We can observe a relatively large simulation error compared with measured data from 40- and 80-cm depth soil in Fig. 8. The measured data show some individual peak value. However, it is difficult to deal with such sudden changes in numerical simulation. From the soil

moisture simulation results at 80-cm depth (Fig. 8), an increase can be seen at the time of 120 days, and the curve fluctuates at a higher level, then decreases to normal level at the time of 270 days. During this period, the soil moisture is quite higher than the actual amount, resulting in more water storage in soil. (2) The accumulation of rainfall and average soil moisture in 1 day through a year were used in the numerical method, which may neglect some details. The amount of daily rainfall seems large during 160 and 255 days (Fig. 5), but the rainfall may be a summation of multiple rain events on that day. These amounts of rainfall can totally infiltrate into the soil and drain from the bottom boundary of the HYDRUS model and generate no surface runoff.

The results show that the sum of the actual evaporation is 587.2 mm in the year, which is far less than the potential evapotranspiration ( $ET_p$ ) with a value of 901.4 mm. The cumulative water fluxes at observation points are presented in

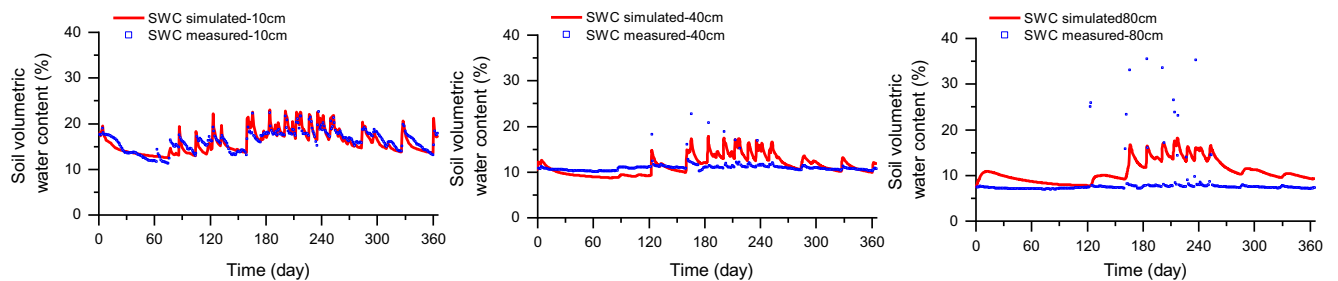


**Fig. 8** Compared to the simulated results of soil volumetric water content with the measured data at different depths

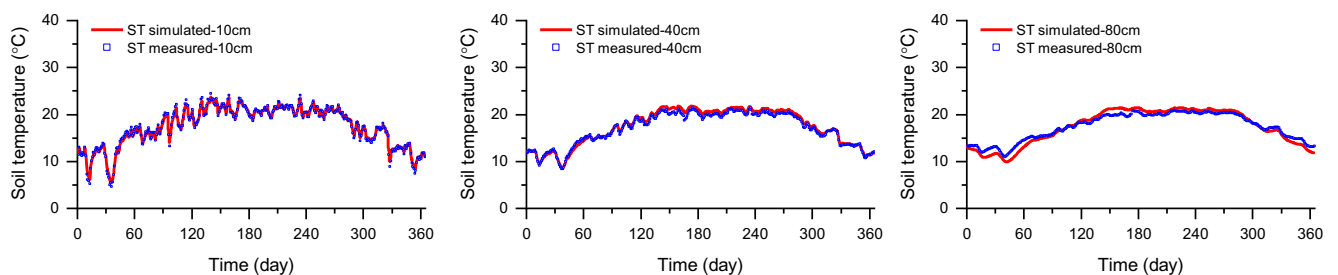


**Fig. 9** Compared the simulated results of soil temperature with the measured data at different depths

**Table 5** The parameters of NSE, RMSE, and RRMSE for the model evaluation (SWC represent the soil water content, ST represent the soil temperature in the table)

SWC	NSE	RMSE	RRMSE	Performance	ST	NSE	RMSE	RRMSE	Performance
$\theta_{10\text{cm}}$	0.73	0.0119	0.105	Excellent	ST <sub>10cm</sub>	0.99	0.32	0.016	Excellent
$\theta_{40\text{cm}}$	-1.78	0.0204	0.161	Good	ST <sub>40cm</sub>	0.98	0.43	0.033	Excellent
$\theta_{80\text{cm}}$	-0.04	0.0377	0.132	Good	ST <sub>80cm</sub>	0.99	0.27	0.027	Excellent

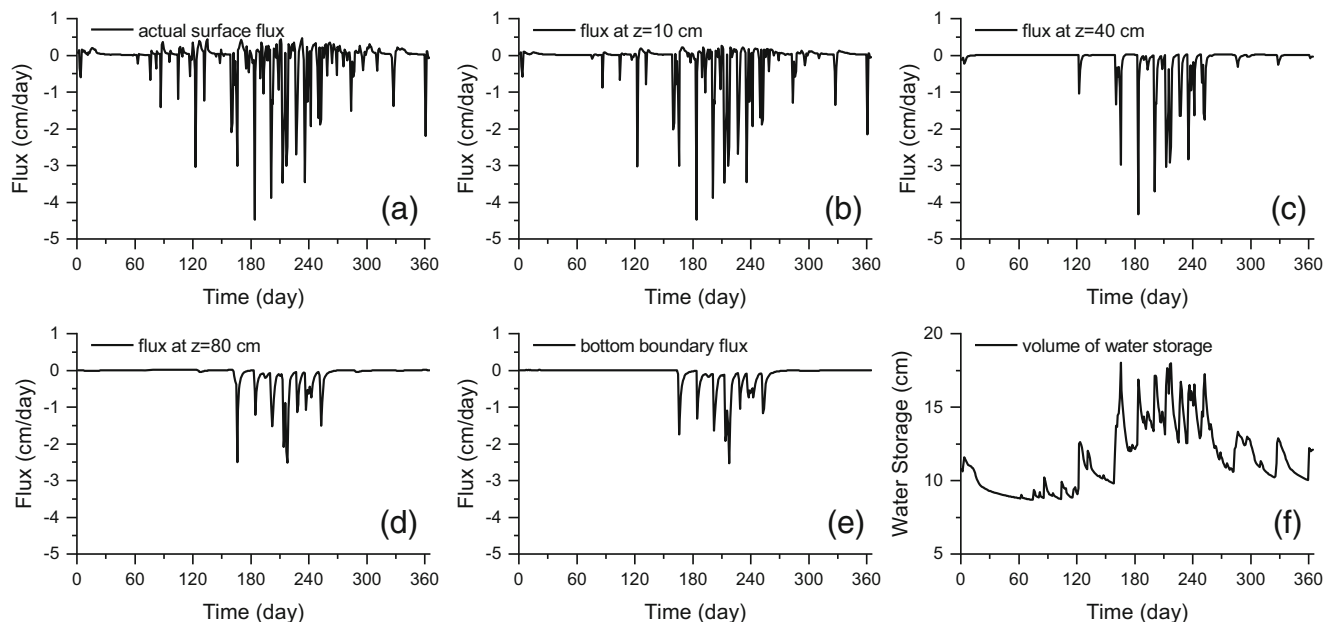
Fig. 11b. It can be noticed that the fluxes are close to zero in the first 150 days, then increase sharply during 150 and 250 days, and eventually tend to be stable after 250 days. The main span for soil water storage is during the days from 150 to 250.

The liquid water and vapor flux along the profile at specified times were visualized in Figs. 12 and 13. The flux is a vector that is positive when water or vapor flows upwards, and vice versa. The liquid water flux is 3–6 orders of magnitude larger than vapor flux. In the theory of soil water heat transfer, Philip and Devries (1957) applied the thermal dynamic equilibrium hypothesis to the process of soil vapor transport and supposed that the soil water vaporizes at one end of the soil pores and condenses at the other end; therefore, the condensation and evaporation rate reach a balance, and the rate equals to water vapor transport flux density. So the soil vapor water is mainly affected by soil thermal gradient and air temperature and soil water pressure head (Philip and Devries 1957; Saito et al. 2006). The liquid water and vapor flux on a specific day can be analyzed with the meteorological and measured soil temperature data as listed in Table 6. For example, at the time  $t = 10$  days, there was no rain on the day but had rain on the previous day, and the potential evapotranspiration was greater than the precipitation, therefore leading to the liquid water

flow upwards at  $z = 40$  cm but downwards between the depth of 40 and 100 cm. However, the vapor flux was always upwards because the soil temperature has upward gradients. Water transport at any time can be analyzed by the above method which can be used as basic evidence for soil water isotopic analysis in isotopic hydrology study.

## Conclusions

The long-term field monitoring of soil moisture and temperature was carried out in the karst rocky desertification area. The water flux along the soil profile and the variation of soil moisture and temperature were studied based on the coupled soil moisture and heat transport model. The conclusions can be drawn as follows: (1) The rainfall is very low on the plateau with the annual cumulative that is 1027.2 mm which concentrates from June to August. Therefore, the surface soil moisture fluctuates rapidly but the deeper soil hardly gets moisture recharged from the rains except for during the heavy rainfall period. The soil temperature is mainly affected by the air temperature and its variation fits the sinusoidal curve perfectly, which

**Fig. 10** a–f The variation of soil water flux with time at different depths and the total volume of water in the model

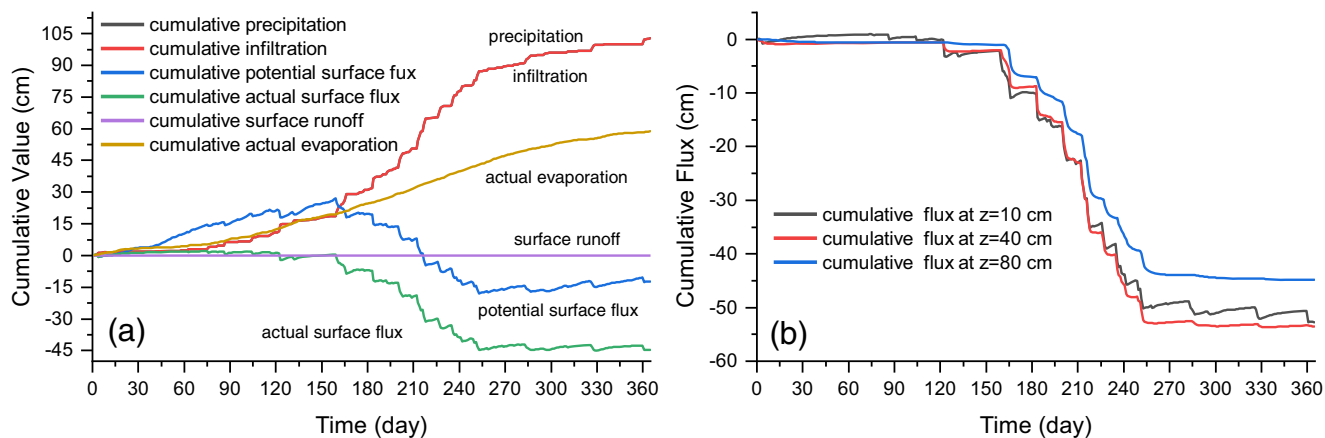


Fig. 11 a–b The cumulative precipitation, infiltration, and water flux at different depths on the profile

implies the intimate relationship to the Earth’s rotation and revolution; (2) the simulated results show a larger error for soil water content while small error for soil temperature. The model performance was evaluated to be good and excellent for SWC and ST, respectively. The model error is within the normal tolerance, and large errors may result from the monitoring and observation error and the igno-

rance of the preferential flow throughout the interface between soil and rock; (3) the analyses of liquid water and vapor flux throughout the soil profile show that there is no surface runoff and the precipitation infiltrates into the soil. In general, the liquid water flux is 3–6 orders of magnitude larger than vapor, but the vapor water transportation has some significance under a drought weather condition.

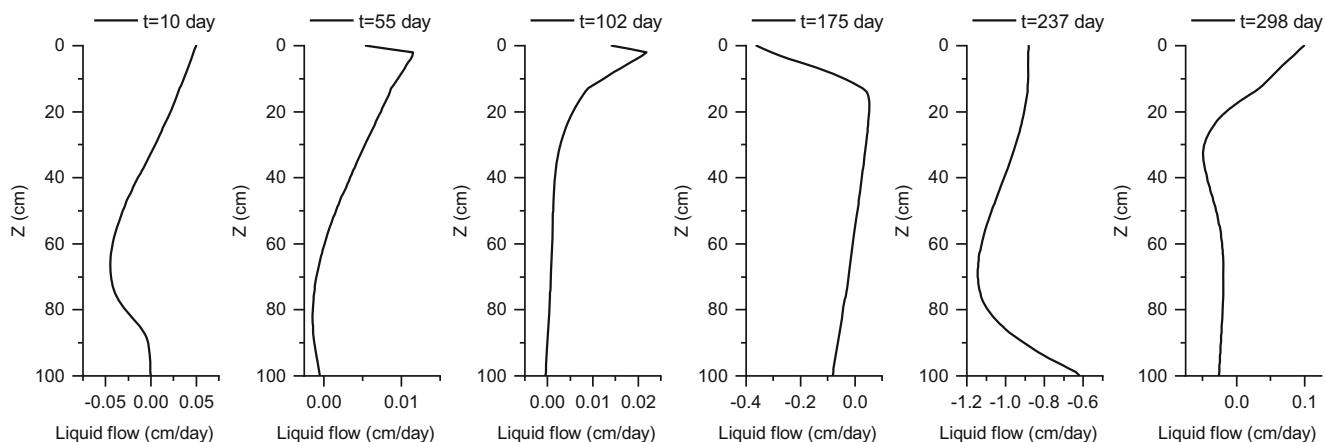


Fig. 12 Liquid water flux curve of soil profile at specified times

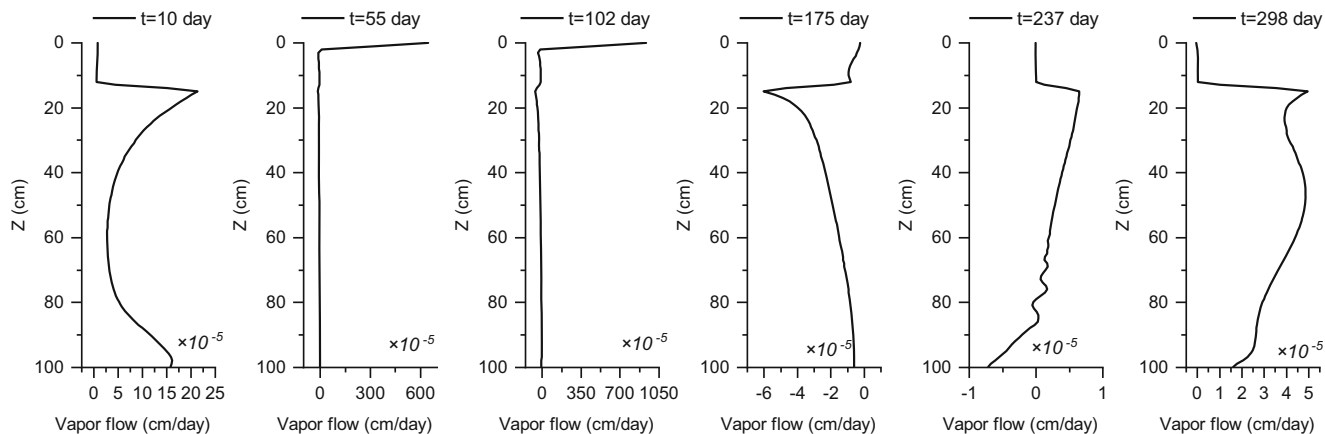


Fig. 13 Vapor water flux curve of the soil profile at specified times



**Table 6** Precipitation, potential evapotranspiration, and soil temperature monitoring data at specified times ( $ET_p$  potential evapotranspiration,  $ST$  soil temperature)

Time (days)	Precipitation (cm/day)	$ET_p$ (cm/day)	$ST_{10cm}$ (°C)	$ST_{40cm}$ (°C)	$ST_{80cm}$ (°C)	Time (days)	Precipitation (cm/day)	$ET_p$ (cm/day)	$ST_{10cm}$ (°C)	$ST_{40cm}$ (°C)	$ST_{80cm}$ (°C)
9	0.04	0.09	11.14	12.42	13.36	174	0.1	0.2	21.80	21.35	20.74
10	0	0.05	7.26	11.89	13.40	175	0.66	0.3	21.81	21.00	20.77
11	0.06	0.07	6.08	10.78	13.32	176	0	0.25	21.83	21.07	20.70
54	0.04	0.19	15.46	14.20	13.70	236	3.56	0.1	20.00	21.07	20.66
55	0	0.3	15.69	14.11	13.92	237	1.02	0.14	19.15	20.09	20.83
56	0	0.32	16.60	14.23	14.01	238	0.08	0.31	20.39	19.89	20.63
101	0	0.45	20.05	17.04	16.46	297	0.3	0.08	14.30	17.15	18.60
102	0	0.52	20.53	17.51	16.64	298	0.02	0.12	15.41	16.64	18.44
103	0	0.54	21.67	17.91	16.84	299	0.14	0.14	16.71	16.71	18.22

Further investigations should consider the preferential flow throughout the rock-soil interface, which would make the model more accurate, and thus the role of rocks in the infiltration process can be discussed in detail. Moreover, we have done some field dye tracer experiments in the study site, and the stable hydrogen and oxygen isotopes for rainfall and soil water are under laboratory detection. All these new data and evidence will contribute to understanding the complex process of water transport and the energy transfer process in karst rocky desertification areas.

**Acknowledgments** We especially thank Prof. Junbing Pu, two anonymous reviewers, and editors for their thoughtful comments and suggestions, which greatly improved the original draft.

**Authors' contributions** Xiaofeng Xiong: conceptualization, methodology, formal analysis, investigation, data curation, methodology, writing-original draft, writing-review and editing. Jianhong Li: conceptualization, formal analysis, investigation, data curation, resources, writing-original draft, writing-review and editing, funding acquisition. Tao Zhang: conceptualization, investigation, methodology, data curation, writing-original draft, writing-review and editing. Sainan Wang: methodology, investigation, writing-original draft, writing-review and editing. Weijie Huo: methodology, investigation, data curation, writing-original draft, writing-review and editing.

**Funding** This study was financially supported by the Key Research & Development Fund of the Ministry of Science and Technology of China (No. 2016YFC0502501) and the Guangxi Natural Science Foundation (2017GXNSFFA198006, 2018GXNSFBA138031).

**Data availability** The datasets used and/or analyzed during the current study are available from the corresponding author on reasonable request.

## Compliance with ethical standards

**Ethical approval and consent to participate** Not applicable.

**Consent for publication** Not applicable.

**Competing interests** The authors declare that they have no conflicts of interest.

## References

- Bai XY, Wang SJ, Xiong KN (2013) Assessing spatial-temporal evolution processes of karst rocky desertification land: indications for restoration strategies. *Land Degrad Dev* 24:47–56. <https://doi.org/10.1002/ldr.1102>
- Bhumralkar CM (1975) Numerical experiments on the computation of ground surface temperature in an atmospheric general circulation model. *Journal of Applied Meteorology* 14:1246–1258. [https://doi.org/10.1175/1520-0450\(1975\)014<1246:NEOTCO>2.0.CO;2](https://doi.org/10.1175/1520-0450(1975)014<1246:NEOTCO>2.0.CO;2)
- Cardololiver R, Kranz M, Smettem KRJ, Mayer K (2005) A reactive soil moisture sensor network: design and field evaluation. *Int J Distrib Sens N* 1:149–162. <https://doi.org/10.1080/15501320590966422>
- Carson JE (1963) Analysis of soil and air temperatures by Fourier techniques. *Journal of Geophysical Research* 68:2217–2232. <https://doi.org/10.1029/JZ068i008p02217>

- Cass A, Campbell GS, Jones TL (1984) Enhancement of thermal water vapor diffusion in soil. *Soil Sci Soc Am J* 48:25–32. <https://doi.org/10.2136/sssaj1984.03615995004800010005x>
- Chen H, Zhang W, Wang K, Fu W (2010) Soil moisture dynamics under different land uses on karst hillslope in northwest Guangxi, China. *Environ Earth Sci* 61:1105–1111. <https://doi.org/10.1007/s12665-009-0428-3>
- Chung S, Horton R (1987) Soil heat and water flow with a partial surface mulch. *Water Resour Res* 23:2175–2186. <https://doi.org/10.1029/WR023i012p02175>
- Dai Q, Peng X, Yang Z, Zhao L (2017) Runoff and erosion processes on bare slopes in the karst rocky desertification area. *Catena* 152:218–226. <https://doi.org/10.1016/j.catena.2017.01.013>
- Davidson EA, Belk E, Boone RD (1998) Soil water content and temperature as independent or confounded factors controlling soil respiration in a temperate mixed hardwood forest. *Glob Change Biol* 4: 217–227. <https://doi.org/10.1046/j.1365-2486.1998.00128.x>
- Dunn PH, Barro SC, Poth M (1985) Soil moisture affects survival of microorganisms in heated chaparral soil. *Soil Biol Biochem* 17: 143–148. [https://doi.org/10.1016/0038-0717\(85\)90105-1](https://doi.org/10.1016/0038-0717(85)90105-1)
- Federer C (1979) A soil-plant-atmosphere model for transpiration and availability of soil water. *Water Resour Res* 15:555–562. DOI/10.1029/WR015i003p00555
- Guo L, Chen J, Lin H (2015) Subsurface lateral preferential flow network revealed by time-lapse ground-penetrating radar in a hillslope. *Water Resour Res* 50:9127–9147. <https://doi.org/10.1002/2013WR014603>
- Hall AE, Kaufmann MR (1975) Regulation of water transport in the soil-plant-atmosphere continuum. *Perspectives of biophysical ecology*. Springer. pp:187–202
- Jackson TJ, Schmugge J, Engman E (1996) Remote sensing applications to hydrology: soil moisture. *Hydrol Sci J-J Sci Hydrol* 41:517–530. <https://doi.org/10.1080/02626669609491523>
- Jarvis N, Koestel J, Larsbo M (2016) Understanding preferential flow in the vadose zone: recent advances and future prospects. *Vadose Zone J* 15. <https://doi.org/10.2136/vzj2016.09.0075>
- Jaynes D (1990) Temperature variations effect on field-measured infiltration. *Soil Sci Soc Am J* 54:305–312. <https://doi.org/10.2136/sssaj1990.03615995005400020002x>
- Jianfeng Y, Shuqin W, Wei D, Guangxin Z (2005) Review of numerical simulation of soil water flow and solute transport in the presence of a water table. *Transactions of the CSAE* 6:158–165. <https://doi.org/10.3321/j.issn:1002-6819.2005.06.036> (in Chinese with English abstract)
- Jiang Y (2011) Strontium isotope geochemistry of groundwater affected by human activities in Nandong underground river system, China. *Appl Geochem* 26(3):371–379. <https://doi.org/10.1016/j.apgeochem.2010.12.010>
- Jiang Z, Lian Y, Qin X (2014) Rocky desertification in Southwest China: impacts, causes, and restoration. *Earth-Sci Rev* 132:1–12 <https://doi.org/10.1016/j.earscirev.2014.01.005>
- Kang S, Kim S, Oh S, Lee D (2000) Predicting spatial and temporal patterns of soil temperature based on topography, surface cover and air temperature. *For Ecol Manage* 136:173–184. [https://doi.org/10.1016/S0378-1127\(99\)00290-X](https://doi.org/10.1016/S0378-1127(99)00290-X)
- Kostov KG, Jackson TJ (1993) Estimating profile soil moisture from surface-layer measurements: a review. *Proceedings of SPIE* 1941: 125–136. <https://doi.org/10.1117/12.154681>
- Li S, Ren H, Xue L, Chang J, Yao X (2014) Influence of bare rocks on surrounding soil moisture in the karst rocky desertification regions under drought conditions. *Catena* 116:157–162. <https://doi.org/10.1016/j.catena.2013.12.013>
- Li S, Birk S, Xue L, Ren H, Chang J, Yao X (2016) Seasonal changes in the soil moisture distribution around bare rock outcrops within a karst rocky desertification area (Fuyuan County, Yunnan Province, China). *Environ Earth Sci* 75:1482. <https://doi.org/10.1007/s12665-016-6290-1>
- Li X, Xu X, Liu W, He L, Zhang R, Xu C, Wang K (2017) Similarity of the temporal pattern of soil moisture across soil profile in karst catchments of southwestern China. *J Hydrol* 555:659–669. <https://doi.org/10.1016/j.jhydrol.2017.10.045>
- Li J, Li J, Pu J, Zhang T, Wang S, Xiong X, Huo W (2019) Effects of light rainfall events on spatial variation of soil moisture and leaf water potential of apple tree (*Malus pumila* Mill.) in a karst graben basin, Yunnan Province. *CARSOLOGICA SINICA*, 38(2) 233–242. <https://doi.org/10.11932/karst20190208> (in Chinese with English abstract)
- Li J, Pu J, Zhang T, Xiong X, Wang S, Huo W, Yuan D (2020) Measurable sediment discharge from a karst underground river in southwestern China: temporal variabilities and controlling factors. *Environ Earth Sci* 79:79–90. <https://doi.org/10.1007/s12665-020-8826-7>
- Luo W, Xu X, Liu W, Liu M, Li Z, Peng T, Xu C, Zhang Y, Zhang R (2019) UAV based soil moisture remote sensing in a karst mountainous catchment. *Catena* 174:478–489. <https://doi.org/10.1016/j.catena.2018.11.017>
- Mahdavi SM, Neyshabouri MR, Fujimaki H, Majnooni Heris A (2017) Coupled heat and moisture transfer and evaporation in mulched soils. *Catena* 151:34–48. <https://doi.org/10.1016/j.catena.2016.12.010>
- Monteith J (1981) Evaporation and surface temperature. *Q J R Meteorol Soc* 107:1–27. <https://doi.org/10.1002/qj.49710745102>
- Mualem Y (1976) A new model for predicting hydraulic conductivity of unsaturated porous media. *Water Resour Res* 12:513–522. <https://doi.org/10.1029/WR012i003p00513>
- Nassar IN, Horton R (1992) Simultaneous transfer of heat, water, and solute in porous media: I. Theoretical development[J]. *Soil Sci Soc Am J* 56(5):1350–1356
- Nemes A, Schaap M, Leij F, Wösten J (2001) Description of the unsaturated soil hydraulic database UNSODA version 2.0. *J Hydrol* 251: 151–162. [https://doi.org/10.1016/S0022-1694\(01\)00465-6](https://doi.org/10.1016/S0022-1694(01)00465-6)
- Nimmo JR, Miller EE (1986) The temperature dependence of isothermal moisture vs. potential characteristics of soils. *Soil Sci Soc Am J* 50: 1105–1113. <https://doi.org/10.2136/sssaj1986.03615995005000050004x>
- Parton WJ, Logan JA (1981) A model for diurnal variation in soil and air temperature. *Agricultural Meteorology* 23:205–216. [https://doi.org/10.1016/0002-1571\(81\)90105-9](https://doi.org/10.1016/0002-1571(81)90105-9)
- Passioura J (1982) Water in the soil-plant-atmosphere continuum. *Physiological plant ecology II*. Springer. pp:5–33
- Philip JR (1966) Plant water relations: some physical aspects. *Annu Rev Plant Biol* 17:245–268. <https://doi.org/10.1146/annurev.pp.17.060166.001333>
- Philip JR, Devries DA (1957) Moisture movement in porous materials under temperature gradient. *Eos Transactions American Geophysical Union* 38:222–232. <https://doi.org/10.1029/TR038i002p00222>
- Qiang L, Pu J, Ni H, Du H, Qi X, Li W, Hui Y, Laboratory KD, Amp M, GZAR (2017) A research approach for ecological, environmental and geological differentiation of rocky desertification and its driving mechanism in karst graben basin. *Advances in Earth Science* 32: 899–907. <https://doi.org/10.11867/j.issn.1001-8166.2017.09.0899> (in Chinese with English abstract)
- Qiu Y, Fu B, Wang J, Chen L (2001) Spatial variability of soil moisture content and its relation to environmental indices in a semi-arid gully catchment of the Loess Plateau, China. *J Arid Environ* 49:723–750. <https://doi.org/10.1006/jare.2001.0828>
- Raes D, Munoz G (2009) The ETo calculator. Reference Manual Version,
- Saito H, Simunek J, Scanlon BR, Reedy RC (2006) Numerical analysis of coupled water, vapor and heat transport in the vadose zone using

- HYDRUS. *Vadose Zone J* 5:784–800. <https://doi.org/10.2136/vzj2006.0007>
- Sala O, Lauenroth W, Parton W (1992) Long-term soil water dynamics in the shortgrass steppe. *Ecology* 73:1175–1181. <https://doi.org/10.2307/1940667>
- Scanlon BR, Keese K, Reedy RC, Simunek J, Andraski BJ (2003) Variations in flow and transport in thick desert vadose zones in response to paleoclimatic forcing (0–90 kyr): field measurements, modeling, and uncertainties. *Water Resour Res* 39. <https://doi.org/10.1029/2002WR001604>
- Seneviratne SI, Corti T, Davin EL, Hirschi M, Jaeger EB, Lehner I, Orlowsky B, Teuling AJ (2010) Investigating soil moisture–climate interactions in a changing climate: a review. *Earth-Sci Rev* 99:125–161. <https://doi.org/10.1016/j.earscirev.2010.02.004>
- Shao M, Horton R, Jaynes D (1998) Analytical solution for one-dimensional heat conduction-convection equation. *Soil Sci Soc Am J* 62:123–128. <https://doi.org/10.2136/sssaj1998.03615995006200010016x>
- Simunek J, Saito H, Sakai M, Genuchten TM (2005) The HYDRUS-1D Software Package for simulating the one-dimensional movement of water, heat, and multiple solutes in variably-saturated media. Hydrus Software. Department of Environmental Sciences University of California Riverside Riverside. pp 11–52
- Šimůnek J, Van Genuchten MT, Šejna M (2012) The HYDRUS software package for simulating the two-and three-dimensional movement of water, heat, and multiple solutes in variably-saturated porous media. Technical manual, version 2:258
- Šimůnek J, Van Genuchten MT, Šejna M (2016) Recent developments and applications of the HYDRUS computer software packages. *Vadose Zone J* 15. <https://doi.org/10.2136/vzj2016.04.0033>
- Smith K, Ball T, Conen F, Dobbie K, Massheder J, Rey A (2018) Exchange of greenhouse gases between soil and atmosphere: interactions of soil physical factors and biological processes. *Eur J Soil Sci* 69:10–20. <https://doi.org/10.1046/j.1351-0754.2003.0567.x>
- Sohrt J, Ries F, Sauter M, Lange J (2014) Significance of preferential flow at the rock soil interface in a semi-arid karst environment. *Catena* 123:1–10. <https://doi.org/10.1016/j.catena.2014.07.003>
- Valipour M, Sefidkouhi MAG, Raeni-Sarjaz M (2017) Selecting the best model to estimate potential evapotranspiration with respect to climate change and magnitudes of extreme events. *Agric Water Manage* 180:50–60. <https://doi.org/10.1016/j.agwat.2016.08.025>
- Van Genuchten MT (1980) A closed-form equation for predicting the hydraulic conductivity of unsaturated soils 1. *Soil Sci Soc Am J* 44:892–898. <https://doi.org/10.2136/sssaj1980.03615995004400050002x>
- Vereecken H, Huisman J, Pachepsky Y, Montzka C, Van Der Kruk J, Bogena H, Weiermüller L, Herbst M, Martinez G, Vanderborght J (2014) On the spatio-temporal dynamics of soil moisture at the field scale. *J Hydrol* 516:76–96. <https://doi.org/10.1016/j.jhydrol.2013.11.061>
- Wang SJ, Liu QM, Zhang DF (2004) Karst rocky desertification in southwestern China: geomorphology, landuse, impact and rehabilitation. *Land Degrad Dev* 15:115–121. <https://doi.org/10.1002/ldr.592>
- Wang J, Gong S, Xu D, Juan S, Mu J (2013) Numerical simulations and validation of water flow and heat transport in a subsurface drip irrigation system using HYDRUS-2D. *Irrig Drain* 62:97–106. <https://doi.org/10.1002/ird.1699>
- Wang S, Pu J, Li J, Zhang T, Huo W, Yuan D (2019) Climatic characteristics under the influence of basin-mountain coupled topography and its influence on the ecological restoration of rocky desertification in Mengzi karst graben basin, Southwest China. *CARSOLOGICA SINICA*, 38(1):50–59. <https://doi.org/10.11932/karst20190106> (in Chinese with English abstract)
- Watlet A, Kaufmann O, Triantafyllou A, Poulain A, Chambers JE, Meldrum PI, Wilkinson PB, Hallet V, Quinif Y, Van RM (2018) Imaging groundwater infiltration dynamics in the karst vadose zone with long-term ERT monitoring. *Hydrol Earth Syst Sci* 22:1563–1592. <https://doi.org/10.5194/hess-22-1563-2018>
- Western AW, Blöschl G (1999) On the spatial scaling of soil moisture. *J Hydrol* 217:203–224. [https://doi.org/10.1016/S0022-1694\(98\)00232-7](https://doi.org/10.1016/S0022-1694(98)00232-7)
- Western AW, Zhou S-L, Grayson RB, McMahon TA, Blöschl G, Wilson DJ (2004) Spatial correlation of soil moisture in small catchments and its relationship to dominant spatial hydrological processes. *J Hydrol* 286:113–134. <https://doi.org/10.1016/j.jhydrol.2003.09.014>
- Wilcox BP, Wood MK, Tromble JM (1988) Factors influencing infiltrability of semiarid mountain slopes. *Journal of Range Management* 41:197–206. <https://doi.org/10.2307/3899167>
- Willmott CJ (1981) On the validation of models. *Phys Geogr* 2:184–194. <https://doi.org/10.1080/02723646.1981.10642213>
- Willmott CJ (1982) Some comments on the evaluation of model performance. *Bull Amer Meteorol Soc* 63:1309–1313. [https://doi.org/10.1175/1520-0477\(1982\)063<1309:SCOTEO>2.0.CO;2](https://doi.org/10.1175/1520-0477(1982)063<1309:SCOTEO>2.0.CO;2)
- Xu CY, Singh V (2001) Evaluation and generalization of temperature-based methods for calculating evaporation. *Hydrol Process* 15:305–319. <https://doi.org/10.1002/hyp.119>
- Yang J, Chen H, Nie Y, Wang K (2019) Dynamic variations in profile soil water on karst hillslopes in Southwest China. *Catena* 172:655–663. <https://doi.org/10.1016/j.catena.2018.09.032>
- Younes A, Mara TA, Fajraoui N, Lehmann F, Belfort B, Beydoun H (2013) Use of global sensitivity analysis to help assess unsaturated soil hydraulic parameters. *Vadose Zone J* 12:1–12. <https://doi.org/10.2136/vzj2011.0150>
- Zhang D, Zhou G (2016) Estimation of soil moisture from optical and thermal remote sensing: a review. *Sensors* 16:1308. <https://doi.org/10.3390/s16081308>
- Zhang S, Lövdahl L, Grip H, Tong Y, Yang X, Wang Q (2009) Effects of mulching and catch cropping on soil temperature, soil moisture and wheat yield on the Loess Plateau of China. *Soil Tillage Res* 102:78–86. <https://doi.org/10.1016/j.still.2008.07.019>
- Zhang J, Chen H, Su Y, Shi Y, Zhang W, Kong X (2011) Spatial variability of surface soil moisture in a depression area of karst region. *Clean-Soil Air Water* 39:619–625. <https://doi.org/10.1002/clen.201000528>
- Zhao Z, Shen Y, Shan Z, Yu Y, Zhao G (2018) Infiltration patterns and ecological function of outcrop runoff in epikarst areas of southern China. *Vadose Zone J* 17. <https://doi.org/10.2136/vzj2017.11.0197>
- Zhuo L, Han D (2016) The relevance of soil moisture by remote sensing and hydrological modelling. *Procedia Engineering* 154:1368–1375. <https://doi.org/10.1016/j.proeng.2016.07.499>

**Publisher's note** Springer Nature remains neutral with regard to jurisdictional claims in published maps and institutional affiliations.